



# Large polaron formation and its effect on electron transport in hybrid perovskites†

Fan Zheng  and Lin-wang Wang\*Cite this: *Energy Environ. Sci.*,  
2019, 12, 1219Received 15th November 2018,  
Accepted 21st February 2019

DOI: 10.1039/c8ee03369b

rsc.li/ees

Many experiments have indicated that a large polaron may be formed in hybrid perovskites, and its existence is proposed to screen the carrier–carrier and carrier–defect scattering, thus contributing to the long lifetime of the carriers. However, a detailed theoretical study of the large polaron and its effect on carrier transport at the atomic level is still lacking. In particular, how strong is the large polaron binding energy? How does its effect compare with the effect of dynamic disorder caused by the A-site molecular rotation? And how does the inorganic sublattice vibration impact the motion of the large polaron? All of these questions are largely unanswered. In this work, using  $\text{CH}_3\text{NH}_3\text{PbI}_3$  as an example, we implement a tight-binding model fitted from density-functional theory to describe the electron large polaron ground state and to understand the large polaron formation and transport at its strong-coupling limit. We find that the formation energy of the large polaron is around  $-12$  meV for the case without dynamic disorder, and  $-55$  meV by including dynamic disorder. By performing the explicit time-dependent wavefunction evolution of the polaron state, together with the rotations of  $\text{CH}_3\text{NH}_3^+$  and vibrations of the  $\text{PbI}_3^-$  sublattice, we studied the diffusion constant and mobility of the large polaron state driven by the dynamic disorder and the sublattice vibration. Two effects of the inorganic sublattice vibrations are found: on one hand, the vibration of the sublattice provides an additional driving force for carrier mobility; on the other hand, the large polaron polarization further localizes the electron, reducing its mobility. Overall, the effect of the large polaron is to slow down the electron mobility by roughly a factor of two. We believe that both dynamic disorder due to rotation of the organic molecule, and large polaron effects induced by the polarization and vibration of the inorganic sublattice, play important roles for the electronic structure and carrier dynamics of the system.

Joint Center for Artificial Photosynthesis and Materials Sciences Division, Lawrence Berkeley National Laboratory, Berkeley, California 94720, USA.

E-mail: lwwang@lbl.gov

† Electronic supplementary information (ESI) available. See DOI: 10.1039/c8ee03369b

## Broader context

Hybrid perovskites have attracted a great deal of research interest, not only because of their high power conversion efficiency for solar cells but also because of the intrinsic new physics that exists in these systems. In particular, the interplays between the A-site molecular reorientation, soft lattice vibration and electron localization have produced novel physical phenomena different from conventional semiconductors. Many investigations have demonstrated the localization of the excited carriers caused by the fast rotation of A-site molecules (dynamic disorder). Meanwhile, other works have shown the strong electron–phonon coupling, hypothesizing the formation of a large polaron. However, an *ab initio* treatment including both dynamic disorder and a large polaron is difficult, and the role of the large polaron in such localized electron systems is still unclear. In this work, by using a large-scale *ab initio* derived tight-binding model, we have directly simulated the effect of the large polaron and the resulting electron diffusion. We have included both lattice screening and dynamic disorder at an equal footing. In addition to the screening, the lattice vibrational contribution to the electron diffusion is also incorporated. Such a model offers a clear understanding of the contributions to the carrier motion due to different effects and lays the groundwork to study the general large polaron formation and transport in hybrid perovskites.

## Introduction

The outstanding performance of hybrid perovskites (HPs) in solar cells has attracted a great number of studies to understand their fundamental physical principles. In addition to the high tolerance for defects,<sup>1–4</sup> the exceptionally long carrier lifetime and diffusion length despite the modest mobility for the excited carriers, have become the most focused research topic.<sup>5–9</sup> Many mechanisms have been proposed to explain such a long carrier lifetime and diffusion length. For example, owing to the dipole moment of the molecules such as  $\text{CH}_3\text{NH}_3^+$  (MA), it has been hypothesized that the polar nature of the molecule introduces the ferroelectricity and polar potential in HPs.<sup>10</sup> It has also been proposed that the ferroelectric domain and domain walls contribute to the fast electron–hole separation and slow recombination.<sup>11–14</sup> Besides, the broken inversion

symmetry can also lead to the so-called Rashba effect under the strong spin-orbit coupling introduced by heavy atoms such as Pb and I. The different spin chiralities and the momentum vectors of the band edge states with spin and momentum mismatch forbid the carrier-recombination in  $k$  space,<sup>15–18</sup> prolonging the lifetime of the excited carriers. However, the ferroelectricity of HPs has been under debate,<sup>19,20</sup> as many works show that these materials could be centrosymmetric at room temperature owing to the fast reorientation of the molecules. In addition, pure inorganic halide perovskite CsPbX<sub>3</sub> also shows similar carrier behavior to the hybrid case.<sup>21,22</sup> Instead of forming a ferroelectric domain, another explanation based on the dipole moment of the MA is dynamic disorder, where the disordered orientation of the molecules exhibits random potential on an inorganic sublattice such as PbI<sub>3</sub><sup>–</sup>. Such varying potential modulates the band edge states of the electrons and holes, and produces spatially localized wavefunctions at different locations on a nano-size scale in real space,<sup>23–26</sup> which suppresses their recombination. Recently, more has been found that both the fast-rotating molecules and the soft inorganic sublattice can affect the carrier transport *via* the strong electron-phonon coupling.<sup>15,27–29</sup> Compared to the conventional direct-band-gap semiconductors such as GaAs, the modest carrier mobility of MAPbI<sub>3</sub> indicates the contribution to the carrier scattering by optical phonon modes.<sup>9,30,31</sup> It is believed that with the relatively strong electron-phonon coupling, a large polaron can be formed to develop pseudo-free dressed carriers, and it can screen them from other carriers and defects to avoid recombination and trapping, which leads to long lifetime and long diffusion length.<sup>32–36</sup>

Large polaron refers to the shallow bound state due to the Coulomb interaction between the charge carrier and the polarizable lattice. The so-called small polaron has been studied in this material, where the wavefunction is strongly localized within the chemical bonds.<sup>35–37</sup> It is believed that the A-site molecules play a significant role in forming the small polarons, and such small polarons are crucial to explain the formation and annihilation of the trap states. However, different from the small polarons, the large polaron often spreads over hundreds of unit cells owing to the relatively weak long-range Coulomb interaction and the small lattice distortion by the longitudinal optical (LO) phonon mode.<sup>38</sup> It is suggested that the long time decay of more than 100 ps for the hot carrier relaxation in the experiments for various HPs,<sup>7,39–41</sup> could be owing to the large polaron screening<sup>39,40,42</sup> (at low excitation density) or the “phonon bottleneck” (at high excitation density caused by the large polaron overlapping).<sup>27,43,44</sup> The Fröhlich model further reveals the size of the large polaron and its transport estimated from a model Hamiltonian.<sup>27</sup> Using the time-resolved optical Kerr effect spectroscopy, the large polaron formation time is estimated to be around 0.3 ps to 0.7 ps in MAPbBr<sub>3</sub> and CsPbBr<sub>3</sub>.<sup>45</sup> A pioneer first-principles calculation with the hybrid exchange–correlation functional has shown the possible formation of large polarons in CsPbBr<sub>3</sub> and MAPbBr<sub>3</sub> along one direction, and has estimated their formation energies to be 140 and 60 meV, respectively.<sup>46</sup> In this calculation, it is observed

that the PbBr<sub>3</sub><sup>–</sup> lattice deforms under the charge of an electron or hole.<sup>46</sup> Due to the large computational cost, the first-principle calculation was only done for one-dimensional polarons, instead of the real three-dimensional case. Owing to the possibility of overestimation of wavefunction delocalization with the LDA or GGA semi-local functional, direct density functional theory (DFT) total energy calculation must be dealt with carefully to avoid self-interaction errors. Furthermore, the previous *ab initio* works only considered the static large polaron effect, without its coupling to the MA molecular rotation, or sublattice vibration. As mentioned earlier, it has been experimentally confirmed that the MA molecules are randomly re-orientating in a sub-picosecond time scale. In our previous work,<sup>24</sup> we have shown that the random orientation of MA causes random potentials, which can localize the electrons and holes at different locations in real space and reduce their recombination. The rotation of MA also induces a dynamic disorder changing with time, providing a driving force for the carrier motion. The time-dependent Schrödinger's equation following the fluctuating potentials yields a carrier mobility, which agrees with the experimental value within its uncertainty range. However, in our previous work, the effects of the PbI<sub>3</sub><sup>–</sup> inorganic sublattice have not been included. This sublattice has two additional potential effects, one is the large polaron bound polarization potential which further localizes the carrier wavefunction; another is the fluctuation of the lattice which provides an additional driving force for the carrier movement.

In this work, we include the large polaron effect together with the dynamic disorder provided by the MA rotations and the vibrations of the PbI<sub>3</sub><sup>–</sup> sublattice. Since the large polaron effect is caused by the Coulomb interaction between the charge carrier and the lattice optical phonons, we construct a tight-binding (TB) model of MAPbI<sub>3</sub><sup>15</sup> following from DFT calculations. As shown previously,<sup>24</sup> such a TB model can describe the carrier localization accurately, reproducing the large-scale DFT calculation results for tens of thousands of atoms. The formation of the polaron as well as its dynamics under the influence of the MA rotation and PbI<sub>3</sub><sup>–</sup> sublattice vibration is simulated directly with a 48 × 48 × 48 supercell system with more than 1 million atoms. Our directly calculated formation energy agrees with the Fröhlich model within the strong coupling approximation. Since the temperature directly influences the rate of the molecular rotation, we compute the diffusion constant of the electron at different molecular re-orientation rates and with different PbI<sub>3</sub><sup>–</sup> sublattice vibrations at different temperatures. The effect of the PbI<sub>3</sub><sup>–</sup> sublattice vibration is modeled with the molecular dynamics of the sublattice, which alters the TB model coupling parameters and on-site potentials. Our calculation suggests that the mobility of the electron is reduced by a factor of 2 by including the polaron and sublattice vibrational effects. However, adding the vibrational effect of the PbI<sub>3</sub><sup>–</sup> sublattice tends to enhance the carrier diffusion more at a high temperature than at a low temperature. The resulting mobility is within the experimental uncertainty when compared with experimental values. By assuming small activation energy for the molecular reorientation rate, we obtain the same trend of mobility with respect to the temperature dependence as the experimental results.

## Large polaron formation

A large polaron in a polarizable crystal is a result of two competing factors. On one hand, the localization of a carrier wavefunction causes a positive kinetic energy scaling as  $1/L^2$  where  $L$  is the size of the localized state. On the other hand, such localized charge will induce the screening of the polarizable crystal lattice, resulting in negative energy due to a charge-polarization interaction scaling as  $-1/L$ . Note that it is important to avoid the erroneous self-interaction that possibly exists in the DFT total energy calculation which also scales as  $1/L$ . In DFT, the exact exchange shall be used to cancel the self-interaction error originated from the Coulomb energy. An incomplete cancellation (if using GGA or LDA) tends to yield a more extended polaron state. However, the TB model used here does not have the Coulomb interaction term, thus no self-interaction error. Without this self-interaction error, for sufficiently large  $L$ , the negative polarization energy will win and the total energy could be lowered compared to the delocalized Bloch state. Therefore, a large polaron can always be formed in a polarizable crystal, although its binding energy may be smaller than the room temperature thermal energy, making it difficult to observe. The most popular large polaron Hamiltonian is proposed by Fröhlich, where the LO phonon model is assumed to couple to the electron wavefunction.<sup>47</sup> The exact Fröhlich model is difficult to solve due to the correlation effect.<sup>38</sup> However, under the strong-coupling approximation, the large polaron wavefunction can be written as a product of the “electron” part and the “ionic” part under the Born–Oppenheimer (BO) approximation. Under this approximation, the total energy of the polaron is obtained by minimizing eqn (1) through the variation of electron wavefunction  $\psi$ :

$$\begin{aligned} E &= \langle \psi | H_0 | \psi \rangle - E^P \\ E^P &= \frac{1}{2\bar{\epsilon}} \int d\mathbf{r} V^P(\mathbf{r}) \rho(\mathbf{r}) \end{aligned} \quad (1)$$

where  $H_0$  is the Hamiltonian of the electron without the polaron effect,  $\rho(\mathbf{r}) = |\psi(\mathbf{r})|^2$  is the charge density for state  $\psi(\mathbf{r})$ ,  $E^P$  indicates the screening energy, and  $V^P$  is the polarization potential of the lattice in response to the Coulomb potential of  $\rho(\mathbf{r})$ . The screening caused by electron–phonon coupling consisting of the ionic contribution of the dielectric constant is represented by  $\bar{\epsilon}$ :  $\frac{1}{\bar{\epsilon}} = \frac{1}{\epsilon_\infty} - \frac{1}{\epsilon_0}$ .  $\epsilon_\infty$  and  $\epsilon_0$  are the electronic and static dielectric constants. Using DFT linear response theory,<sup>48–53</sup> we have calculated  $\epsilon_\infty$  as 4.5, and  $\epsilon_0$  as 21. When the electron wavefunction is self-trapped in real space, it induces a distortion of the lattice to provide a polarization potential, which self-consistently localizes the electron wavefunction. Here, by expressing the electron energy with  $\langle \psi | H_0 | \psi \rangle$ , we avoid the self-interaction energy error. On the other hand, the screening of  $\psi$  due to another electron is represented by the  $\epsilon_\infty$  in the expression of  $\bar{\epsilon}$ . By minimizing the total energy of eqn (1) with respect to the wavefunction, we obtain

the Hamiltonian:

$$H|\psi\rangle = \left( H_0 - \frac{1}{\bar{\epsilon}} V^P[\rho] \right) |\psi\rangle = \epsilon |\psi\rangle \quad (2)$$

where  $V^P$  depends on the charge density  $\rho$  as  $V^P(\mathbf{r}) = \int d\mathbf{r}' \frac{\rho(\mathbf{r}')}{|\mathbf{r} - \mathbf{r}'|}$ .

To achieve self-consistency, an iterative scheme is used to solve the Hamiltonian by updating the wavefunction and polarization potential for every iteration. Since the electron charge density  $\rho$  is localized in a relatively large area (e.g. 50 Å), a macroscopic dielectric constant  $\bar{\epsilon}$  can be used to describe its screening effect.

Due to the large size of large polarons, we use a supercell of  $48 \times 48 \times 48$  (corresponding to more than 300 Å lattice), which is large enough to model a polaron and its transport. Apparently, such a large system is beyond the reach of DFT. Since we are only interested in the conduction band edge for the electron, a tight-binding (TB) model with nearest-neighbor hopping is used to construct a Hamiltonian (see ESI†).<sup>15</sup> In this TB model, the onsite energy and hopping magnitude are fitted to the DFT calculated band structures. The TB parameters are listed in the ESI.† These fitted parameters are also consistent with the Hamiltonian obtained using the maximally localized Wannier function representation.<sup>54</sup> Here, owing to its significance to the electronic structure,<sup>16,55,56</sup> the spin–orbit coupling (SOC) is also included in the TB model<sup>57</sup> and the DFT calculations. As one can see in Fig. S1 of the ESI,† the TB model reproduces well the DFT band edge electronic structures. Due to the sparse nature of the TB Hamiltonian, the parallelized ARPACK<sup>58</sup> math library is used to solve the eigenstates. The ARPACK packages also allow us to solve the interior eigenstates of the Hamiltonian. To solve eqn (2) self-consistently, we start with a localized wavefunction  $\psi$  (for example, with a Gaussian-shape initial potential), and iterate through the self-consistent equation until both kinetic energy ( $\langle \psi | H_0 | \psi \rangle$ ) and potential energy ( $E^P$ ) are converged.

Fig. 1a shows the charge density of the large polaron state and its polarization potential  $V^P/\bar{\epsilon}$  (Fig. 1b) when we ignore the dynamic disorder potential due to the random orientation of the MA molecules. By comparing the energies with and without the large polaron effect, our TB calculation reveals that the formation energy of the large polarons in such a crystal is about  $-12$  meV. In a Fröhlich model, a dimensionless coupling constant  $\alpha$  is often used to quantify the electron–phonon coupling strength:

$$\alpha = \frac{e^2}{\hbar} \frac{1}{4\pi\epsilon} \left( \frac{1}{\epsilon_\infty} - \frac{1}{\epsilon_0} \right) \sqrt{\frac{m^*}{2\hbar\omega_{\text{LO}}}} \quad (3)$$

where  $\omega_{\text{LO}}$  is the LO phonon frequency, and  $m^* = 0.25$  is the effective mass of the electrons (or  $m^* = 0.55$  for holes), fitted from the DFT band structure. In particular, our phonon calculation and other work<sup>59–61</sup> show that there exist low energy LO phonons, corresponding to the  $\text{PbI}_3^-$  sublattice vibrations. We average the phonon frequencies weighed by their contribution to the low-frequency dielectric constant and acquire  $\omega_{\text{LO}} = 2.39$  THz (ESI†). This value is consistent with both

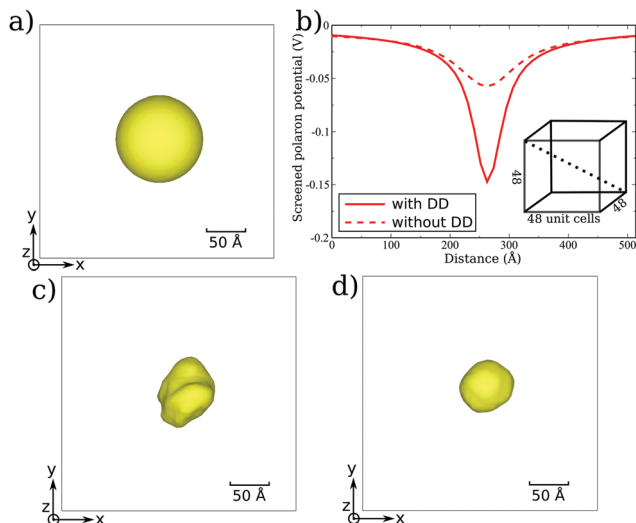


**Fig. 1** (a) The conduction band minimum (CBM) state (charge density) with the large polaron effect (for cleanliness, all the atoms in this big supercell are not shown). (b) The screened polaron polarization potential  $V^P/\epsilon$  along the diagonal line of the cubic supercell (the diagonal line is shown in the inset diagram) for the case with and without the dynamic disorder (DD) effect. (c) The localized CBM state (charge density) induced by the DD without a large polaron effect. (d) The CBM state (charge density) under a large polaron effect and DD. These states are plotted so that more than 85% charge is enclosed in the isosurface. The charge near the boundary of the supercell is negligible, showing that the size of the supercell is large enough.

experimental<sup>29</sup> and theoretical<sup>62,63</sup> work. Using this phonon frequency, the  $\alpha$  is estimated as 3.24, which is in line with other halide ionic crystals such as CsI ( $\alpha = 3.67$ ), RbCl ( $\alpha = 3.81$ ) or oxide perovskite  $\text{SrTiO}_3$  ( $\alpha = 3.77$ ).<sup>64,65</sup> The large  $\alpha$  of  $\text{MAPbI}_3$  falls in the low-end region of the strong coupling. This picture is further supported by the recent experiment that reported the formation of a strong-coupling polaron in the HP.<sup>66</sup> Within the strong-coupling approximation, the polaron formation energy can be computed as  $E = -0.106\alpha^2\hbar\omega_{\text{LO}} = -11$  meV,<sup>47,67</sup> which agrees well with our direct TB modeling result. Here, the specific value of  $\omega_{\text{LO}}$  does not influence the Fröhlich calculated binding energy, since it has been canceled in the above formula and eqn (3). Meanwhile, the polaron state (charge density) can be fitted to a Gaussian function. Thus, if defining the size of the polaron as the deviation of the Gaussian function ( $\bar{r} \equiv \sigma$ ), the radius of the polaron states obtained from the TB model is estimated to be 28 Å. This is also consistent with 32 Å computed based on the Fröhlich model at the strong-coupling limit with the Gaussian approximation.<sup>67</sup>

As demonstrated in ref. 24, the disordered MA molecular orientation produces potential variations on Pb and I atoms due to their dipole moments. Such random molecular potentials lead to the localized conduction band minimum (CBM) and valence band maximum (VBM) in the real space with a nano-size scale as shown in Fig. 1c. This is a localized state before considering the large polaron effect, where the random potential is described inside  $H_0$ . By adding the large polaron effect as the second term in eqn (1), it further localizes the

charge shown in Fig. 1d. A polaron size of around 50 Å has been obtained. Compared to the large polaron without the dynamic disorder (Fig. 1a), the charge density is much more localized. It is also more localized compared to the case of the dynamic disorder without the large polaron effect (Fig. 1c). The solid line in Fig. 1b indicates the converged polarization potential along the diagonal line of the super cell for the large polaron state under dynamic disorder. The maximum amplitude of this potential is 0.15 eV, which is similar to the dynamic disorder potential fluctuation which is around 0.2 eV as shown in Fig. S4 (ESI<sup>†</sup>).<sup>24</sup> However, this potential is more narrow compared with the dynamic disorder potential fluctuation. The additional large polaron binding energy is about -55 meV. This binding energy is much larger than the -12 meV binding energy in the case without dynamic disorder. This is because the dynamic disorder already pre-localizes the electron wavefunction. Using this polarization potential, the spatial displacements of ions in generating such polarization could be estimated based on their Born-effective charge (ESI<sup>†</sup>). We estimate that such displacement is on average on the order of 0.001 Å, which is smaller than the thermal fluctuations around 0.01–0.1 Å.

## Polaron transport

In our previous work,<sup>24</sup> it is suggested that the transport of the excited electron is mainly driven by the molecular rotation induced dynamic disorder. When a molecule changes its orientation, its electric static potential on the neighboring Pb and I atoms is altered. The aforementioned localized CBM state can “hop” to a new state once its energy crosses the energy of another state. In this work, in order to model such a dynamical process with a large polaron effect (*i.e.* the polarization screening effect due to the  $\text{PbI}_3^-$  sublattice), the Monte-Carlo (MC) simulation of the MA rotation is performed with a rotation rate taken from experimental measurements. For each MC step, the total energy difference is computed by summing over the screened dipole–dipole interactions between the molecules. This energy difference is used to accept or reject trial rotations. In our model, molecular dipoles are interacting with each other *via* the screened dipole–dipole interaction with the screening coming from the inorganic  $\text{PbI}_3^-$  sublattice. The total energy by summing over dipole  $\mathbf{d}$  at site- $m$  is expressed as:

$$E_{\text{tot}} = \sum_m d_m \cdot \tilde{\mathbf{E}}_m$$

$$\tilde{\mathbf{E}}_m = \frac{1}{\epsilon_n} \sum_n \mathbf{E}_m(n) + \frac{1}{\epsilon_{n'}} \sum_{n'} \mathbf{E}_m(n') + \frac{1}{\epsilon_{n''}} \sum_{n''} \mathbf{E}_m(n'') \quad (4)$$

$$+ \frac{1}{\epsilon_{n'''}} \sum_{n'''} \mathbf{E}_m(n''')$$

where  $\tilde{\mathbf{E}}_m$  is the screened electric field from other dipoles applied to the dipole at site  $m$ . Here, we believe that dipoles at different distances will have a different screening effect from the  $\text{PbI}_3^-$  sublattice in order to mimic the reciprocal-vector dependent screening. Therefore, we partition the spatial summation into

four different layers ( $n$ : nearest neighbor;  $n'$ : next-nearest neighbor;  $n''$ : third-nearest neighbor;  $n'''$ : others) with different dielectric constants.  $\epsilon_{n'''}$  is known as 21, corresponding to the low frequency dielectric constant  $\epsilon_0$ . Besides the electric field, the average potential at the MA molecule sites  $\left( V_m = \frac{1}{\epsilon_n} \sum_n V_m(n) + \frac{1}{\epsilon_{n'}} \sum_{n'} V_m(n') + \frac{1}{\epsilon_{n''}} \sum_{n''} V_m(n'') + \frac{1}{\epsilon_{n'''}} \sum_{n'''} V_m(n''') \right)$  is screened with the same set of dielectric constants. The dielectric constants ( $\epsilon_n$ ,  $\epsilon_{n'}$ , and  $\epsilon_{n''}$ ) are obtained by fitting the potentials computed from the above screened dipole-dipole model to the averaged potentials of a molecule extracted from the DFT calculations (ESI<sup>†</sup>) with many random configurations of the MA molecules. For a given MA orientation configuration, the  $\text{PbI}_3^-$  sublattice is fully relaxed. Thus, the DFT potential contains the screening effect of the  $\text{PbI}_3^-$  sublattice, as described in eqn (4). Fig. 2 shows the comparison of the potential obtained between the above model and DFT potential, which demonstrates the validity of our screening model.

After each MC step, their potentials on each Pb and I atom are re-evaluated. Between two MC steps, the potential change is interpolated linearly into small time steps ( $\sim 0.048$  fs) in order to carry out the evolution of the wavefunction. The time-dependent wavefunction evolution is solved following Schrodinger's equation by applying the evolution operator to the wavefunction directly:

$$\begin{aligned} \psi(t+dt) &= e^{-iH(t)dt} \psi(t) \\ &\approx \left[ 1 - iH(t)dt - \frac{1}{2}H^2(t)dt^2 + \frac{i}{6}H^3(t)dt^3 + \frac{1}{24}H^4(t)dt^4 \right] \psi(t) \end{aligned} \quad (5)$$

The evolution operator is expanded up to the fourth order of  $dt$  to ensure the convergence of the evolution regarding  $dt$ . Here,  $H$  is defined in eqn (2).

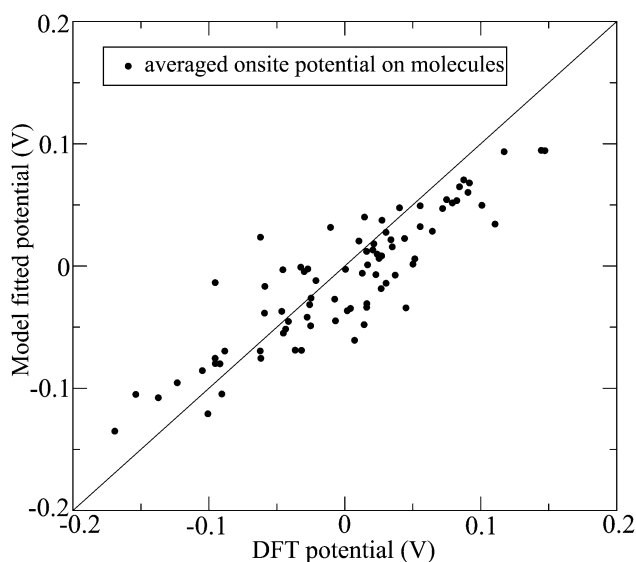


Fig. 2 The comparison between the potentials calculated using DFT and the fitted layer-dependent dipole-dipole screening potential.

With the setup of eqn (5), now we can consider the effects of the large polaron. Two effects are associated with the  $\text{PbI}_3^-$  sublattice. The first is the change of polarization following the change of charge density  $\rho(\mathbf{r})$ ; the second is the thermal fluctuation of the  $\text{PbI}_3^-$  sublattice. We first consider the polarization change. The  $\text{PbI}_3^-$  sublattice polarization will follow the movement of  $\rho(\mathbf{r}) = |\psi(\mathbf{r})|^2$ . However, such polarization by lattice distortion is not instantaneous; instead, some sub-picosecond time is needed to form a large polaron as discussed before. Thus, when the electron hops from one location to a new location, the change of the lattice screening owing to the new charge density will also be retarded. To represent this effect, we mix the old polarization potential and the new potential with a ratio weighted by the evolution time and the polaron formation time as:

$$V_{t_{n+1}}^P = V_{t_{n+1}}^{\text{Poisson}}[\rho_{t_{n+1}}] \left( 1 - e^{-\frac{dt}{\tau}} \right) + V_{t_n}^P e^{-\frac{dt}{\tau}} \quad (6)$$

where  $V^{\text{Poisson}}$  is the instantaneous polarization potential calculated from the Poisson solver with a charge density  $\rho_{t_{n+1}}$ ,  $\tau$  is the large polaron formation/annihilation time, and  $dt = t_{n+1} - t_n$ . The resulting  $V_{t_{n+1}}^P$  is used for the second term in  $H$  of eqn (2). In the experiment, the polaron formation time has been estimated to be around 0.3 and 0.7 ps for  $\text{MAPbBr}_3$  and  $\text{CsPbBr}_3$ , respectively. There is no estimation of  $\tau$  for  $\text{MAPbI}_3$ . In our simulation, we have tested  $\tau = 0$  fs, 80 fs, 150 fs and 300 fs, and large  $\tau$  only slightly reduced the diffusion constant (ESI<sup>†</sup>). However, the reduction is quite small compared to other factors discussed below. Thus, we have used  $\tau = 80$  fs for our calculations. Such retarded potential is then added to the Hamiltonian and the wavefunction evolution.

With this in place, now we can study the effects of the polaron on carrier diffusion. In our dynamical simulation, the time step  $dt$  for the wavefunction evolution is 2 a.u. (around 0.048 fs) to ensure its stability. For every ten  $dt$  steps, an MC step is applied to rotate the molecules. To capture the change of the polaron polarization potential, the Poisson equation is re-solved based on the charge density for every 5 fs. To quantify the diffusion process,  $R^2(t)$  has been calculated as shown by Fig. 3a, where  $R^2(t) = \langle \psi(t) | (\mathbf{r} - \mathbf{r}_0)^2 | \psi(t) \rangle$  is evaluated for the localized wavefunctions.  $\mathbf{r}_0$  is the center of mass of the charge density at  $t = 0$ . The initial wavefunction square  $|\psi|^2(t = 0)$  is shown as Fig. 1d. To illustrate the wavefunction evolution, we show the states at  $t = 900$  fs for a given trajectory shown in Fig. 3a with and without the large polaron effect in Fig. 3b and c, respectively. We can see that the originally localized CBM state in the center of the box starts to diffuse off center in the case with dynamic disorder and a large polaron. For the case with dynamic disorder only, the wavefunction has been broken down into a few pieces. In order to further quantify the diffusion of the large polaron, we perform 20 independent trajectories starting from the same initial state with different random MC seeds, with and without the large polaron effect. The  $R^2(t)$  of all 20 trajectories are shown in Fig. 3a. For the case without a polaron, the carrier can quickly escape from the

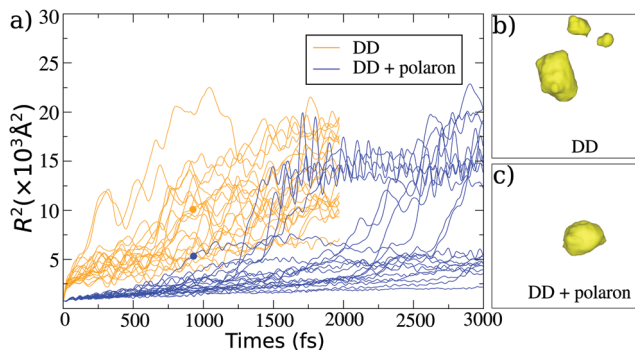


Fig. 3 (a)  $R^2(t)$  of 20 independent trajectories for the case (orange line) with dynamic disorder only (DD) and the case (blue line) with both dynamic disorder and a large polaron. The molecular rotation time used in this graph is 6 ps. (b) Snapshot of the wavefunction (charge density) for the case with dynamic disorder only at time  $t = 900$  fs. This state is picked up from the trajectory with an orange dot in (a). (c) Snapshot of the wavefunction (charge density) for the case with dynamic disorder and the large polaron effect at time  $t = 900$  fs. This state is picked up from the trajectory with a blue dot in (a).

center after 200 fs from the initial state. Moreover, once the carrier is hopped away, its  $R^2$  value oscillates strongly, indicating a strong spatial variation of the wavefunction in real space. However, by including the polaron effect, some of the trajectories have very small increments even after a long time. This corresponds to the situation that these localized states are still in the center and do not get a chance to hop. In general, the carrier needs to spend more than 1 ps before it can accumulate enough potential variations in order to overcome the initial polarization potential and hop to a different place. Once the carrier is moved, it tends to stay in a new place for a while before jumping to another location, showing a step-like  $R^2$ . But the important conclusion is that the polarization potential does not completely trap the carrier in a location permanently. The carrier can still

move and hop to a new place, although this hopping rate is smaller than the case without the large polaron effect. By averaging  $R^2(t)$  for all the trajectories, we compute the diffusion coefficient  $D$  as  $\bar{R}^2(t) = \langle R^2(t) \rangle = 6Dt$ .<sup>24</sup> The averaged  $R^2(t)$  forms a straight line as we expected (Fig. 4a), and the slope of this straight line yields the diffusion constant  $D$ . By doing so for each rotation rate, we obtain Fig. 4b, where the diffusion constants are compared for the case with dynamic disorder only and the case with dynamic disorder and large polaron polarization (but without yet the thermal fluctuation of the  $\text{PbI}_3^-$  sublattice). The diffusion constants without the large polaron effect agree with our previous results in ref. 24, although some modifications have been made both for the TB model and the screening model of eqn (4). The large polaron reduces the diffusion coefficient by a factor of 2. This is because the additional polaron polarization potential further localizes the wavefunction and deepens the localization potential, thus makes the hopping more difficult.

Up to now, we have discussed the effects of the large polaron and A-site molecular orientation flipping induced dynamic disorder to the carrier dynamics. Besides forming the polarization potential in response to the carrier charge density, the thermal vibrations of the  $\text{PbI}_3^-$  sublattice can also exert a driving force to induce the carrier motion in addition to the dynamic disorder potential fluctuation. Such thermal vibrational effects can be represented by the variation of the Pb and I onsite potentials and the change of the TB coupling strength between two neighboring Pb and I atoms. Unfortunately, there is no easy realistic calculation to capture both effects at the same time. Instead, we have used a model dynamics to describe the onsite energy fluctuation, and a classical MD to simulate the structural distortion which results in the change of TB coupling strength. Note that here, the Pb and I onsite potential fluctuation refers to the fluctuation caused by the thermal movement of Pb and I atoms, and not the fluctuation caused

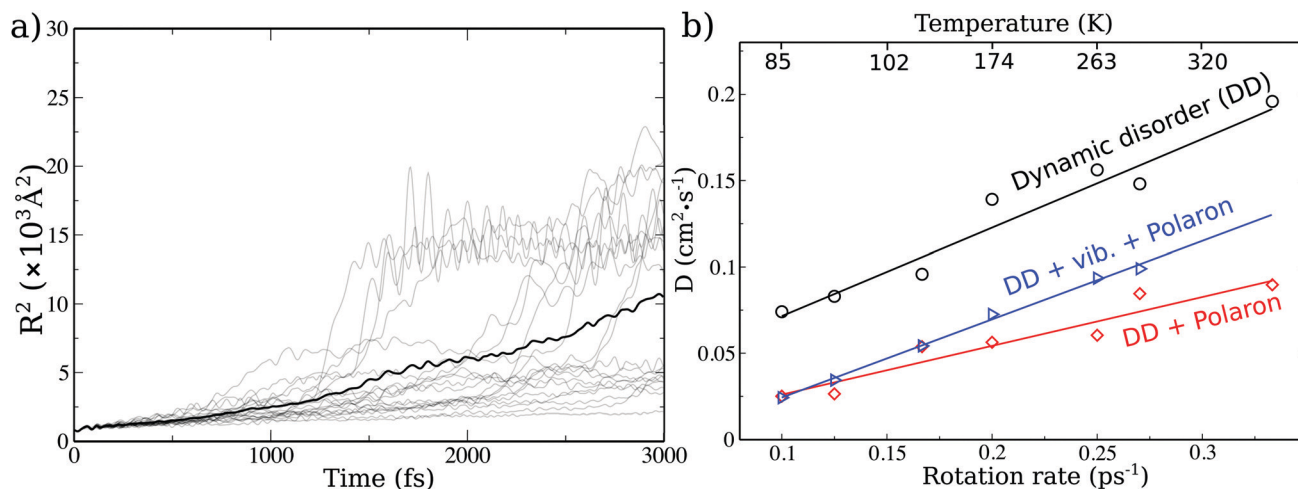


Fig. 4 (a) The  $R^2(t)$  evolution over time for 20 independent trajectories (grey lines) under rotation time at 6 ps. The thick black line indicates the averaged value of the 20 trajectories  $\bar{R}^2(t)$ . (b) The diffusion constant  $D$  obtained for different rotation rates for the three cases: dynamic disorder (DD) only, DD + large polaron, DD +  $\text{PbI}_3^-$  sublattice vibration + large polaron. The temperature  $T$  used in the lattice vibration and MC simulation of DD is correlated with the rotation rate as: rate  $\propto e^{-(10 \text{ meV}/kT)}$ .<sup>24</sup>

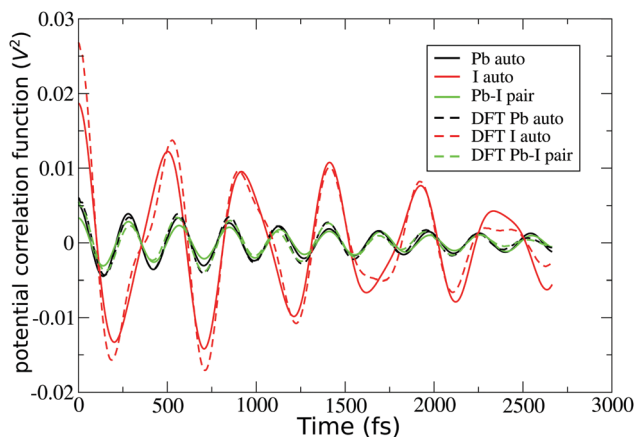


Fig. 5 The Pb autocorrelation, I autocorrelation, and neighboring Pb-I pair correlation functions computed from the Langevin model dynamics and DFT *ab initio* MD.

by the MA molecular rotations, which has been already included in the dynamic disorder model. This statistic feature of the onsite potential fluctuation can be collected from a small supercell *ab initio* MD while fixing the MA molecules. Fig. 5 shows the averaged Pb-, I- onsite auto-correlation function and nearest neighboring Pb-I pair potential correlation functions, obtained from a DFT trajectory (ESI<sup>†</sup>) with fixed MA molecules. The relatively simple oscillations of the DFT onsite potential auto-correlation functions allow us to fit it with an onsite Langevin dynamics model comprising simple oscillators. In this model dynamics, the equation of motion for one Pb or I is expressed as  $\ddot{x} = -c\dot{x} - kx + F_{\text{random}}$ ,  $x$  is the variable to describe the dynamics of the potential, parameters  $c$  and  $k$  control the damping rate and oscillation frequency respectively, and  $F_{\text{random}}$  is the random force applied to each Langevin step. These dynamic models are carried out independently for each atom with different parameters for Pb and I sites, denoting their results as  $x_i^{\text{Pb}}(t)$  and  $x_i^{\text{I}}(t)$ , and  $i$  indicates the lattice site. To yield the correct nearest-neighbor Pb-I correlation function, we also mix the dynamics of neighboring Pb and I as follows:  $V_i^{\text{Pb}}(t) =$

$$\alpha_1 x_i^{\text{Pb}}(t) + \beta_1 \sum_{\text{neigh}} x_j^{\text{I}}(t), \quad V_i^{\text{I}}(t) = \alpha_2 x_i^{\text{I}}(t) + \beta_2 \sum_{\text{neigh}} x_j^{\text{Pb}}(t), \quad \text{here}$$

$V_i^{\text{Pb}}(t)$  and  $V_i^{\text{I}}(t)$  are the final Pb and I onsite potential to be added in  $H_0$  with  $\alpha$  and  $\beta$  as fitting parameters. All the parameters used in the model and the mixing weights are tuned so that both the onsite auto-correlation function and neighboring-pair correlation functions of  $V_i^{\text{Pb}}(t)$  and  $V_i^{\text{I}}(t)$  match DFT as shown in Fig. 5. Using this model dynamics, the full onsite potential time evolution profiles of all the Pb and I atoms in the  $48 \times 48 \times 48$  supercell can be obtained. Meanwhile, in order to simulate the  $\text{PbI}_3^-$  sublattice vibration and thus its effects on TB coupling, we performed the classical MD with LAMMPS<sup>68</sup> using the force field designed for  $\text{MAPbI}_3$  for the  $48 \times 48 \times 48$  supercell at different temperatures<sup>69</sup> (ESI<sup>†</sup>). Our tight-binding model is capable of evaluating the change of the hopping strength based on the Pb-I bond-length deviation with the general form  $h = h_0 e^{-\lambda(b-b_0)}$ , where  $h_0$  and  $b_0$  are the equilibrium hopping strength and bond

length, respectively. Here,  $\lambda$  of different bond types are given from ref. 70, where they are fitted by the Wannierization of a large number of structures with different bond distortions.

With the onsite potential and the local TB coupling parameter time evolution profiles for the  $48 \times 48 \times 48$  supercell, the  $\text{PbI}_3^-$  sublattice thermal vibration effect is added to the time-evolution of the wavefunctions described by eqn (5). All these effects are included in the  $H_0$  of eqn (2). Owing to the relatively slow change of the onsite potential and bond length by phonons, we update the  $\text{PbI}_3^-$  structure and the corresponding parameters for every 5 fs. During the 5 fs, the onsite energies and the hoppings are interpolated linearly to small  $dt$  to evolve the wavefunction. To investigate the sublattice vibrational effects at different temperatures, we have calculated the diffusion constants at different temperatures including the effects of the dynamic disorder, large polaron and sublattice vibration as shown in Fig. 4. In Fig. 4, we have used the MA molecular rotation rate as the horizontal axis while using a rate  $\gamma \propto e^{-E_a/kT}$  by assuming the MA rotation activation energy  $E_a = 10$  meV to correlate between different MA rotation rates and temperature  $T$ .<sup>24</sup> Intuitively, the sublattice vibration should enhance the carrier diffusion for all the temperatures, because the onsite potential variation and TB coupling strength change tend to offer additional random driving force for the carrier movement in addition to the dynamic disorder caused by molecular re-orientation. However, our simulation shows that such an effect is not homogeneous at different rotation rates. At high rotation rate (also high temperature), the enhancement of carrier mobility is obvious. While, at low rotation rate (low temperature), the increase is less pronounced. We think that this is because there are actually two possible effects of the  $\text{PbI}_3^-$  sublattice vibration, similar to that of the MA molecule re-orientation. The fluctuation caused by the  $\text{PbI}_3^-$  sublattice vibration can also further localize the carrier, in addition to providing the movement driving force. Such enhanced localization introduces deeper polaron polarization potential, and tends to slow down the carrier motion. This is illustrated in Fig. S6 (ESI<sup>†</sup>), where the minimum value of polaron potentials are extracted. By rotating exactly the same molecular dipoles every MC step for the two cases with and without the  $\text{PbI}_3^-$  sublattice vibrational effect, the polarization potential difference is purely caused by the sublattice vibrations, and this effect deepens the polarization potential. It seems that the two effects of the  $\text{PbI}_3^-$  vibration are competing with each other. Perhaps at a higher temperature, the driving force effect dominates; hence it increases the carrier diffusion, while at a lower temperature, these two effects cancel each other out.

After the diffusion constant is obtained, the mobility can be evaluated by  $\mu = D/k_B T$ . However, the carrier mobilities vary widely from different experiments<sup>30</sup> (Fig. 6). Even for the mobilities measured with the same method, their values could be quite different. Therefore, it is very difficult to compare with the experiments directly. Our calculated mobility is found to be close to the experimental value. By adding the polaron effect, the mobility of the carriers is reduced by half. However, the effect of the  $\text{PbI}_3^-$  sublattice vibration tends to shift up the

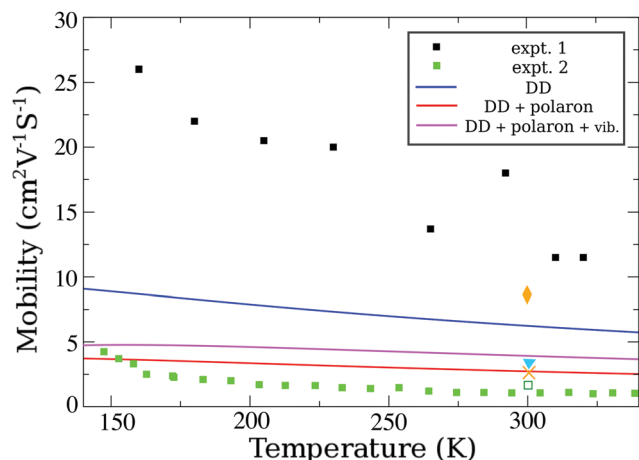


Fig. 6 The calculated mobility with respect to the temperature considering different effects: dynamic disorder (DD) only, DD + large polaron, DD + large polaron +  $\text{PbI}_3^-$  phonon. The experimental values are from ref. 71 for expt 1 and ref. 72 for expt 2. Other experimental measured mobilities are also listed,  $\times$ : ref. 73 ( $\mu_e$ ),  $\nabla$ : ref. 74 ( $\mu_e$ ),  $\square$ : ref. 75 ( $\mu_e + \mu_h$ ),  $\diamond$ : ref. 76 ( $\mu_e + \mu_h$ ).

mobility, into the range of 3 to 5  $\text{cm}^2 \text{V}^{-1} \text{s}^{-1}$  at the molecular rotation rate between 3 ps to 10 ps. Overall, our results agree with the experiments as we have shown for comparison,<sup>71,72</sup> in particular for the trend. If we fit the temperature-mobility dependence to the relation  $\mu \propto T^k$  for the full temperature range,  $k = -0.523$  (DD),  $-0.448$  (DD + polaron), and  $-0.318$  (DD + polaron + vib) are obtained. Similar to the measured mobilities, the values of  $k$  could be quite different. Many experiments have yielded  $k \approx -1.5$ <sup>71,72,77,78</sup> fitted for tetragonal phase only or together with orthogonal phases, but other values such as  $k = -2.8$  ( $e^-$ ) and  $-2.0$  ( $h^+$ ) are also obtained.<sup>79</sup> However, the dynamic disorder effect caused by the molecules becomes more prominent at a high temperature. At a low temperature, the rotation of the molecules is further constrained by the  $\text{PbI}_3$  sublattice, and their orientation becomes more ordered,<sup>80</sup> which may suppress the carrier localization. Meanwhile,  $\epsilon_0$  could have strong temperature dependence at a low temperature, which alters the polaron polarization screening. Therefore, if we fit  $k$  only in a high-temperature range (for example  $> 290$  K), we obtain  $k = -0.65$  (DD),  $-0.63$  (DD + polaron), and  $-0.55$  (DD + polaron + vib). This result is in line with  $k = -0.42$ , fitted from the measured mobilities of experiment 2<sup>72</sup> at a high-temperature range ( $> 290$  K). Recent theoretical work<sup>62</sup> also achieved a  $k$  value around  $-0.46$ , consistent with what we get. Considering the differences of experiments 1 and 2, in experiment 1,<sup>71</sup> they used the PL and THz conductivity spectra to study the temperature-dependent mobility. In experiment 2,<sup>72</sup> the time-resolved microwave conductivity technique was used to explore the effect of A-site cations on the carrier dynamics. The reason for the large difference between the two experiments could be complicated; it might depend on the sample conditions due to different synthesis conditions *etc.* If we assume the sample conditions to be the same, then the better agreement with experiment 2 could be because the electric field used in the microwave probe is weak,<sup>72</sup> which is consistent with the weak field limit in our calculation.

The strong electric field in THz measurement may introduce the non-linear mobility effect, as the potential drop caused by each hopping is in the same order as the potential barrier for the wavefunction localization. Furthermore, the THz frequency time is similar to the phonon frequency, which in some degree might freeze the lattice polarization in its measurement. As a result, its measured mobility might be more close to our previous study without large polaron effects, as shown in Fig. 6. In our current simulation, the A-site is occupied by polar molecules. For pure inorganic halide perovskite such as  $\text{CsPbX}_3$ , the displacement of the  $\text{Cs}^+$  atom contributes to the formation of the large polarons. However, without the slow rotational degree of freedom of the A-site molecule, the large polaron may be hard to form, and it will have a much smaller binding energy. This may explain the higher mobility observed in  $\text{CsPbBr}_3$ .<sup>26,72,81</sup> In this work, the large polaron of the hole is not discussed. However, as shown in our previous work,<sup>23</sup> the electron and hole are localized at different locations due to the potential fluctuation caused by the random orientation of the MA molecule. The large polaron tends to further localize them, thus their reduced spatial overlap may lower the radiative recombination and enhance the lifetime.

In the end, we want to justify the hopping picture and the BO approximation we have used throughout this work. There have been continuous efforts to understand the large polaron in hybrid perovskites, *e.g.* using the Bloch state as the starting point to include the scattering of optical phonon modes.<sup>31</sup> For a conventional perfect crystal structure such as GaAs with a weak electron-phonon coupling, the Boltzmann equation is more appropriate to describe the large polaron transport with the Bloch state as a starting point,<sup>82</sup> although there are also attempts to use the hopping picture for large polaron transport even in a perfect crystal,<sup>83</sup> However, the hybrid perovskites including  $\text{MAPbI}_3$  are not a usual “perfect crystal”. Recent experiments and theoretical work have shown the strong electron-phonon coupling and indicated that the carrier could be localized under the random orientation of the A-site molecules, which is also the reason why these materials are unusual and fascinating. Under this circumstance, the charge is already localized before any additional large polaron induced localization. Thus, the hopping picture of such localized charge is more appropriate to study their transport. This is different from the hopping picture used for small polarons, where the localized states hop between nearby bonds within a unit cell. In this work, the hopping distance is typically comparable to the localization size, thus much larger than the nearest neighbor atomic distance. As for the BO approximation, when the electron-phonon coupling is small (weak-coupling limit, such as GaAs), the phonon affects the electronic structure in a perturbed way. The electron and phonon are correlated dynamically, and the BO approximation is unsuitable. However, when the electron-phonon interaction is strong (strong-coupling limit), the phonon cannot respond to the fast electron movement to necessitate the correlated perturbation treatment. Therefore, the adiabatic BO approximation can be used, as discussed in this work. Another important reason for the BO approximation is that, as discussed above, the wavefunction is already localized under dynamic disorder before

any polaron effect, which will significantly reduce the correlation effect. As we show in our paper, the polaron binding energy for a localized electron becomes much larger. Under our adiabatic approximation, these two localizations (caused by large polaron and dynamic disorder) are treated on equal footing, and there is no approximation between them (not treating one as a perturbation to another). Of course, the perfect method to solve the large polaron at any coupling is to use Feynman's path integral. But this is still difficult to apply to a realistic system at the atomic level.

## Summary

In summary, by using the tight-binding model fitted to first-principles DFT calculations, we studied the large polaron formation and its effects on the carrier transport in MAPbI<sub>3</sub>. We provide an atomic and quantitative picture to understand the large polaron effect in MAPbI<sub>3</sub>. We studied two effects of the PbI<sub>3</sub><sup>-</sup> sublattice on the carrier mobility. The first is the large polaron polarization effect, which tends to further localize the carrier wavefunction on top of the dynamic disorder caused by the MA molecule rotation. The second is the thermal vibration of the PbI<sub>3</sub><sup>-</sup> sublattice which provides randomness to further localize the wavefunction, but also a driving force for carrier movement. Our calculation shows a large polaron with the formation energy around -12 meV for one electron carrier when there is no molecular disorder, which is consistent with the Fröhlich model at a strong coupling limit. By adding dynamic disorder, the large polaron binding energy is increased to -55 meV. This polaron state is accomplished by a lattice polarization potential around 0.14 eV, only slightly smaller than the 0.2 eV potential fluctuation caused by the MA molecular random orientation. By solving the time-dependent Schrodinger's equation and performing MC simulation, we study how the electron state evolves under the driving force of the molecular re-orientation and the lattice vibration. We find that the polaron effect slows down the mobility of the electrons by a factor of 2. On the other hand, the PbI<sub>3</sub><sup>-</sup> sublattice vibration enhances the electron mobility particularly at a high temperature. Overall, the computed mobility is in line with the experimental measurements. Our calculation reveals how the large polaron state is formed and its role in carrier movement in the MAPbI<sub>3</sub> system.

## Conflicts of interest

There are no conflicts to declare.

## Acknowledgements

This article is based on the work performed by the Joint Center for Artificial Photosynthesis, a DOE Energy Innovation Hub, supported by the Office of Science of the U.S. Department of Energy under Award number DE-SC0004993. We used the resources of the National Energy Research Scientific Computing Center (NERSC) located in the Lawrence Berkeley National

Laboratory and the computational resource of the Oak Ridge Leadership Computing Facility at the Oak Ridge National Laboratory under the Innovative and Novel Computational Impact on Theory and Experiment project. We thank Liang Z. Tan, Shi Liu, and Andrew Rappe for the discussions and their help in using the TB model used in this work. We also thank Alessandro Mattoni for the discussions and his help in the classical MD simulation.

## References

- 1 A. Buin, P. Pietsch, J. Xu, O. Voznyy, A. H. Ip, R. Comin and E. H. Sargent, Materials Processing Routes to Trap-Free Halide Perovskites, *Nano Lett.*, 2014, **14**, 6281–6286.
- 2 J. Kim, S.-H. Lee, J. H. Lee and K.-H. Hong, The Role of Intrinsic Defects in Methylammonium Lead Iodide Perovskite, *J. Phys. Chem. Lett.*, 2014, **5**, 1312–1317.
- 3 J. Kang and L.-W. Wang, High Defect Tolerance in Lead Halide Perovskite CsPbBr<sub>3</sub>, *J. Phys. Chem. Lett.*, 2017, **8**, 489–493.
- 4 W.-J. Yin, T. Shi and Y. Yan, Unusual Defect Physics in CH<sub>3</sub>NH<sub>3</sub>PbI<sub>3</sub> Perovskite Solar Cell Absorber, *Appl. Phys. Lett.*, 2014, **104**, 063903.
- 5 T. M. Brenner, D. A. Egger, L. Kronik, G. Hodes and D. Cahen, Hybrid Organic–inorganic Perovskites: Low-Cost Semiconductors with Intriguing Charge-Transport Properties, *Nat. Rev. Mater.*, 2016, **1**, 15007.
- 6 S. D. Stranks, G. E. Eperon, G. Grancini, C. Menelaou, M. J. P. Alcocer, T. Leijtens, L. M. Herz, A. Petrozza and H. J. Snaith, Electron-Hole Diffusion Lengths Exceeding 1 Micrometer in an Organometal Trihalide Perovskite Absorber, *Science*, 2013, **342**, 341–344.
- 7 H. Zhu, K. Miyata, Y. Fu, J. Wang, P. P. Joshi, D. Niesner, K. W. Williams, S. Jin and X.-Y. Zhu, Screening in Crystalline Liquids Protects Energetic Carriers in Hybrid Perovskites, *Science*, 2016, **353**, 1409–1413.
- 8 Q. Dong, Y. Fang, Y. Shao, P. Mulligan, J. Qiu, L. Cao and J. Huang, Electron-Hole Diffusion Lengths > 175 μm in Solution-Grown CH<sub>3</sub>NH<sub>3</sub>PbI<sub>3</sub> Single Crystals, *Science*, 2015, **347**, 967–970.
- 9 T. M. Brenner, D. A. Egger, A. M. Rappe, L. Kronik, G. Hodes and D. Cahen, Are Mobilities in Hybrid Organic–Inorganic Halide Perovskites Actually “High”? *J. Phys. Chem. Lett.*, 2015, **6**, 4754–4757.
- 10 J. M. Frost, K. T. Butler, F. Brivio, C. H. Hendon, M. van Schilfgaarde and A. Walsh, Atomistic Origins of High-Performance in Hybrid Halide Perovskite Solar Cells, *Nano Lett.*, 2014, **14**, 2584–2590.
- 11 S. Liu, F. Zheng, N. Z. Koocher, H. Takenaka, F. Wang and A. M. Rappe, Ferroelectric Domain Wall Induced Band Gap Reduction and Charge Separation in Organometal Halide Perovskites, *J. Phys. Chem. Lett.*, 2015, **6**, 693–699.
- 12 S. N. Rashkeev, F. El-Mellouhi, S. Kais and F. H. Alharbi, Domain Walls Conductivity in Hybrid Organometallic Perovskites and Their Essential Role in CH<sub>3</sub>NH<sub>3</sub>PbI<sub>3</sub> Solar Cell High Performance, *Sci. Rep.*, 2015, **5**, 11467.
- 13 Y.-F. Chen, Y.-T. Tsai, D. M. Bassani and L. Hirsch, Experimental Evidence of the Anti-Parallel Arrangement of

- Methylammonium Ions in Perovskites, *Appl. Phys. Lett.*, 2016, **109**, 213504.
- 14 J. M. Frost, K. T. Butler and A. Walsh, Molecular Ferroelectric Contributions to Anomalous Hysteresis in Hybrid Perovskite Solar Cells, *APL Mater.*, 2014, **2**, 081506.
  - 15 F. Zheng, L. Z. Tan, S. Liu and A. M. Rappe, Rashba Spin-Orbit Coupling Enhanced Carrier Lifetime in  $\text{CH}_3\text{NH}_3\text{PbI}_3$ , *Nano Lett.*, 2015, **15**, 7794–7800.
  - 16 J. Even, L. Pedesseau and C. Katan, Comment on “Density Functional Theory Analysis of Structural and Electronic Properties of Orthorhombic Perovskite  $\text{CH}_3\text{NH}_3\text{PbI}_3$ ” by Y. Wang *et al.*, *Phys. Chem. Chem. Phys.*, 2014, **16**, 1424–1429 (*Phys. Chem. Chem. Phys.*, 2014, **16**, 8697–8698).
  - 17 C. Motta, F. El-Mellouhi, S. Kais, N. Tabet, F. Alharbi and S. Sanvito, Revealing the Role of Organic Cations in Hybrid Halide Perovskite  $\text{CH}_3\text{NH}_3\text{PbI}_3$ , *Nat. Commun.*, 2015, **6**, 7026.
  - 18 T. Etienne, E. Mosconi and F. De Angelis, Dynamical Origin of the Rashba Effect in Organohalide Lead Perovskites: A Key to Suppressed Carrier Recombination in Perovskite Solar Cells?, *J. Phys. Chem. Lett.*, 2016, **7**, 1638–1645.
  - 19 Y. Rakita, O. Bar-Elli, E. Meirzadeh, H. Kaslasi, Y. Peleg, G. Hodes, I. Lubomirsky, D. Oron, D. Ehre and D. Cahen, Tetragonal  $\text{CH}_3\text{NH}_3\text{PbI}_3$  Is Ferroelectric, *Proc. Natl. Acad. Sci. U. S. A.*, 2017, **114**, E5504–E5512.
  - 20 Z. Fan, J. Xiao, K. Sun, L. Chen, Y. Hu, J. Ouyang, K. P. Ong, K. Zeng and J. Wang, Ferroelectricity of  $\text{CH}_3\text{NH}_3\text{PbI}_3$  Perovskite, *J. Phys. Chem. Lett.*, 2015, **6**, 1155–1161.
  - 21 S. Dastidar, S. Li, S. Y. Smolin, J. B. Baxter and A. T. Fafarman, Slow Electron–Hole Recombination in Lead Iodide Perovskites Does Not Require a Molecular Dipole, *ACS Energy Lett.*, 2017, **2**, 2239–2244.
  - 22 O. Yaffe, Y. Guo, L. Z. Tan, D. A. Egger, T. Hull, C. C. Stoumpos, F. Zheng, T. F. Heinz, L. Kronik, M. G. Kanatzidis, J. S. Owen, A. M. Rappe, M. A. Pimenta and L. E. Brus, Local Polar Fluctuations in Lead Halide Perovskite Crystals, *Phys. Rev. Lett.*, 2017, **118**, 136001.
  - 23 J. Ma and L.-W. Wang, Nanoscale Charge Localization Induced by Random Orientations of Organic Molecules in Hybrid Perovskite  $\text{CH}_3\text{NH}_3\text{PbI}_3$ , *Nano Lett.*, 2015, **15**, 248–253.
  - 24 J. Ma and L.-W. Wang, The Nature of Electron Mobility in Hybrid Perovskite  $\text{CH}_3\text{NH}_3\text{PbI}_3$ , *Nano Lett.*, 2017, **17**, 3646–3654.
  - 25 F. Ambrosio, J. Wiktor, F. D. Angelis and A. Pasquarello, Origin of Low Electron–hole Recombination Rate in Metal Halide Perovskites, *Energy Environ. Sci.*, 2018, **11**, 101–105.
  - 26 J. Kang and L.-W. Wang, Dynamic Disorder and Potential Fluctuation in Two-Dimensional Perovskite, *J. Phys. Chem. Lett.*, 2017, **8**, 3875–3880.
  - 27 J. M. Frost, L. D. Whalley and A. Walsh, Slow Cooling of Hot Polarons in Halide Perovskite Solar Cells, *ACS Energy Lett.*, 2017, **2**, 2647–2652.
  - 28 H. Kawai, G. Giorgi, A. Marini and K. Yamashita, The Mechanism of Slow Hot-Hole Cooling in Lead-Iodide Perovskite: First-Principles Calculation on Carrier Lifetime from Electron–Phonon Interaction, *Nano Lett.*, 2015, **15**, 3103–3108.
  - 29 A. D. Wright, C. Verdi, R. L. Milot, G. E. Eperon, M. A. Pérez-Osorio, H. J. Snaith, F. Giustino, M. B. Johnston and L. M. Herz, Electron–Phonon Coupling in Hybrid Lead Halide Perovskites, *Nat. Commun.*, 2016, **7**, 11755.
  - 30 L. M. Herz, Charge-Carrier Mobilities in Metal Halide Perovskites: Fundamental Mechanisms and Limits, *ACS Energy Lett.*, 2017, **2**, 1539–1548.
  - 31 Z.-G. Yu, Rashba Effect and Carrier Mobility in Hybrid Organic–Inorganic Perovskites, *J. Phys. Chem. Lett.*, 2016, **7**, 3078–3083.
  - 32 X.-Y. Zhu and V. Podzorov, Charge Carriers in Hybrid Organic–Inorganic Lead Halide Perovskites Might Be Protected as Large Polarons, *J. Phys. Chem. Lett.*, 2015, **6**, 4758–4761.
  - 33 C. G. Bischak, C. L. Hetherington, H. Wu, S. Aloni, D. F. Ogletree, D. T. Limmer and N. S. Ginsberg, Origin of Reversible Photoinduced Phase Separation in Hybrid Perovskites, *Nano Lett.*, 2017, **17**, 1028–1033.
  - 34 T. Ivanovska, C. Dionigi, E. Mosconi, F. De Angelis, F. Liscio, V. Morandi and G. Ruani, Long-Lived Photoinduced Polarons in Organohalide Perovskites, *J. Phys. Chem. Lett.*, 2017, **8**, 3081–3086.
  - 35 A. J. Neukirch, W. Nie, J.-C. Blancon, K. Appavoo, H. Tsai, M. Y. Sfeir, C. Katan, L. Pedesseau, J. Even, J. J. Crochet, G. Gupta, A. D. Mohite and S. Tretiak, Polaron Stabilization by Cooperative Lattice Distortion and Cation Rotations in Hybrid Perovskite Materials, *Nano Lett.*, 2016, **16**, 3809–3816.
  - 36 E. Welch, L. Scolfaro and A. Zakhidov, Density Functional Theory + U Modeling of Polarons in Organohalide Lead Perovskites, *AIP Adv.*, 2016, **6**, 125037.
  - 37 W. Nie, J.-C. Blancon, A. J. Neukirch, K. Appavoo, H. Tsai, M. Chhowalla, M. A. Alam, M. Y. Sfeir, C. Katan, J. Even, S. Tretiak, J. J. Crochet, G. Gupta and A. D. Mohite, Light-Activated Photocurrent Degradation and Self-Healing in Perovskite Solar Cells, *Nat. Commun.*, 2016, **7**, 11574.
  - 38 R. P. Fzvnman, Institute, C. Slow Electrons in a Polar Crystal, 6.
  - 39 D. Niesner, H. Zhu, K. Miyata, P. P. Joshi, T. J. S. Evans, B. J. Kudisch, M. T. Trinh, M. Marks and X.-Y. Zhu, Persistent Energetic Electrons in Methylammonium Lead Iodide Perovskite Thin Films, *J. Am. Chem. Soc.*, 2016, **138**, 15717–15726.
  - 40 Z. Guo, Y. Wan, M. Yang, J. Snaider, K. Zhu and L. Huang, Long-Range Hot-Carrier Transport in Hybrid Perovskites Visualized by Ultrafast Microscopy, *Science*, 2017, **356**, 59–62.
  - 41 M. B. Price, J. Butkus, T. C. Jellicoe, A. Sadhanala, A. Briane, J. E. Halpert, K. Broch, J. M. Hodgkiss, R. H. Friend and F. Deschler, Hot-Carrier Cooling and Photoinduced Refractive Index Changes in Organic–inorganic Lead Halide Perovskites, *Nat. Commun.*, 2015, **6**, 8420.
  - 42 Z. Zhu, J. Ma, Z. Wang, C. Mu, Z. Fan, L. Du, Y. Bai, L. Fan, H. Yan, D. L. Phillips and S. Yang, Efficiency Enhancement of Perovskite Solar Cells through Fast Electron Extraction: The Role of Graphene Quantum Dots, *J. Am. Chem. Soc.*, 2014, **136**, 3760–3763.

- 43 J. Yang, *et al.*, Acoustic-Optical Phonon up-Conversion and Hot-Phonon Bottleneck in Lead-Halide Perovskites, *Nat. Commun.*, 2017, **8**, 14120.
- 44 Y. Yang, D. P. Ostrowski, R. M. France, K. Zhu, J. van de Lagemaat, J. M. Luther and M. C. Beard, Observation of a Hot-Phonon Bottleneck in Lead-Iodide Perovskites, *Nat. Photonics*, 2016, **10**, 53–59.
- 45 K. Miyata, T. L. Atallah and X.-Y. Zhu, Lead Halide Perovskites: Crystal-Liquid Duality, Phonon Glass Electron Crystals, and Large Polaron Formation, *Sci. Adv.*, 2017, **3**, e1701469.
- 46 K. Miyata, D. Meggiolaro, M. T. Trinh, P. P. Joshi, E. Mosconi, S. C. Jones, F. D. Angelis and X.-Y. Zhu, Large Polarons in Lead Halide Perovskites, *Sci. Adv.*, 2017, **3**, e1701217.
- 47 H. Fröhlich, Electrons in Lattice Fields, *Adv. Phys.*, 1954, **3**, 325–361.
- 48 W. Jia, Z. Cao, L. Wang, J. Fu, X. Chi, W. Gao and L.-W. Wang, The Analysis of a Plane Wave Pseudopotential Density Functional Theory Code on a GPU Machine, *Comput. Phys. Commun.*, 2013, **184**, 9–18.
- 49 W. Jia, J. Fu, Z. Cao, L. Wang, X. Chi, W. Gao and L.-W. Wang, Fast Plane Wave Density Functional Theory Molecular Dynamics Calculations on Multi-GPU Machines, *J. Comput. Phys.*, 2013, **251**, 102–115.
- 50 J. P. Perdew, K. Burke and M. Ernzerhof, Generalized Gradient Approximation Made Simple, *Phys. Rev. Lett.*, 1996, **77**, 3865.
- 51 F. Zheng, J. A. Brehm, S. M. Young, Y. Kim and A. M. Rappe, Substantial Optical Dielectric Enhancement by Volume Compression in LiAsSe<sub>2</sub>, *Phys. Rev. B*, 2016, **93**, 195210.
- 52 D. R. Hamann, Optimized Norm-Conserving Vanderbilt Pseudopotentials, *Phys. Rev. B: Condens. Matter Mater. Phys.*, 2013, **88**, 085117.
- 53 P. Giannozzi, *et al.*, QUANTUM ESPRESSO: A Modular and Open-Source Software Project for Quantum Simulations of Materials, *J. Phys.: Condens. Matter*, 2009, **21**, 395502.
- 54 N. Marzari, A. A. Mostofi, J. R. Yates, I. Souza and D. Vanderbilt, Maximally Localized Wannier Functions: Theory and Applications, *Rev. Mod. Phys.*, 2012, **84**, 1419–1475.
- 55 F. Zheng, H. Takenaka, F. Wang, N. Z. Koocher and A. M. Rappe, First-Principles Calculation of the Bulk Photovoltaic Effect in CH<sub>3</sub>NH<sub>3</sub>PbI<sub>3</sub> and CH<sub>3</sub>NH<sub>3</sub>PbI<sub>3-x</sub>Cl<sub>x</sub>, *J. Phys. Chem. Lett.*, 2015, **6**, 31–37.
- 56 A. Amat, E. Mosconi, E. Ronca, C. Quarti, P. Umari, M. K. Nazeeruddin, M. Grätzel and F. De Angelis, Cation-Induced Band-Gap Tuning in Organohalide Perovskites: Interplay of Spin-Orbit Coupling and Octahedra Tilting, *Nano Lett.*, 2014, **14**, 3608–3616.
- 57 M. Kim, J. Im, A. J. Freeman, J. Ihm and H. Jin, Switchable  $S = 1/2$  and  $J = 1/2$  Rashba Bands in Ferroelectric Halide Perovskites, *Proc. Natl. Acad. Sci. U. S. A.*, 2014, **111**, 6900–6904.
- 58 K. J. Maschhoff and D. C. Sorensen, P\_ARKPACK: An efficient portable large scale eigenvalue package for distributed memory parallel architectures, in *Applied Parallel Computing Industrial Computation and Optimization. PARA 1996. Lecture Notes in Computer Science*, ed. J. Waśniewski, J. Dongarra, K. Madsen and D. Olesen, Springer, Berlin, Heidelberg, 1996, vol. 1184.
- 59 O. Yaffe, Y. Guo, L. Z. Tan, D. A. Egger, T. Hull, C. C. Stoumpos, F. Zheng, T. F. Heinz, L. Kronik, M. G. Kanatzidis, J. S. Owen, A. M. Rappe, M. A. Pimenta and L. E. Brus, Local Polar Fluctuations in Lead Halide Perovskite Crystals, *Phys. Rev. Lett.*, 2017, **118**, 136001.
- 60 M. Sendner, P. K. Nayak, D. A. Egger, S. Beck, C. Müller, B. Epding, W. Kowalsky, L. Kronik, H. J. Snaith, A. Pucci and R. Lovrinčić, Optical Phonons in Methylammonium Lead Halide Perovskites and Implications for Charge Transport, *Mater. Horiz.*, 2016, **3**, 613–620.
- 61 T. Kirchartz, T. Markvart, U. Rau and D. A. Egger, Impact of Small Phonon Energies on the Charge-Carrier Lifetimes in Metal-Halide Perovskites, 2018, arXiv:1801.02169[cond-mat].
- 62 J. M. Frost, Calculating Polaron Mobility in Halide Perovskites, *Phys. Rev. B*, 2017, **96**, 195202.
- 63 M. A. Pérez-Osorio, R. L. Milot, M. R. Filip, J. B. Patel, L. M. Herz, M. B. Johnston and F. Giustino, Vibrational Properties of the Organic-Inorganic Halide Perovskite CH<sub>3</sub>NH<sub>3</sub>PbI<sub>3</sub> from Theory and Experiment: Factor Group Analysis, First-Principles Calculations, and Low-Temperature Infrared Spectra, *J. Phys. Chem. C*, 2015, **119**, 25703–25718.
- 64 E. A. Muljarov and R. Zimmermann, Exciton Dephasing in Quantum Dots Due to LO-Phonon Coupling: An Exactly Solvable Model, *Phys. Rev. Lett.*, 2007, **98**, 187401.
- 65 G. Verbist, F. M. Peeters and J. T. Devreese, Extended Stability Region for Large Bipolarons through Interaction with Multiple Phonon Branches, *Ferroelectrics*, 1992, **130**, 27–34.
- 66 K. Zheng, M. Abdellah, Q. Zhu, Q. Kong, G. Jennings, C. A. Kurtz, M. E. Messing, Y. Niu, D. J. Gosztola, M. J. Al-Marri, X. Zhang, T. Pullerits and S. E. Canton, Direct Experimental Evidence for Photoinduced Strong-Coupling Polarons in Organolead Halide Perovskite Nanoparticles, *J. Phys. Chem. Lett.*, 2016, **7**, 4535–4539.
- 67 J. T. Devreese, *Frohlich Polarons*, Lecture Course Including Detailed Theoretical Derivations, 2016, arXiv preprint arXiv:1611.06122.
- 68 S. Plimpton, Fast parallel algorithms for short-range molecular dynamics, *J. Comput. Phys.*, 1995, **117**, 1–19.
- 69 A. Mattoni, A. Filippetti, M. I. Saba and P. Delugas, Methylammonium Rotational Dynamics in Lead Halide Perovskite by Classical Molecular Dynamics: The Role of Temperature, *J. Phys. Chem. C*, 2015, **119**, 17421–17428.
- 70 M. Z. Mayers, L. Z. Tan, D. A. Egger, A. M. Rappe and D. R. Reichman, How Lattice and Charge Fluctuations Control Carrier Dynamics in Halide Perovskites, *Nano Lett.*, 2018, **18**, 8041–8046.
- 71 R. L. Milot, G. E. Eperon, H. J. Snaith, M. B. Johnston and L. M. Herz, Temperature-Dependent Charge-Carrier Dynamics in CH<sub>3</sub>NH<sub>3</sub>PbI<sub>3</sub> Perovskite Thin Films, *Adv. Funct. Mater.*, 2015, **25**, 6218–6227.
- 72 M. C. Gélvez-Rueda, D. H. Cao, S. Patwardhan, N. Renaud, C. C. Stoumpos, G. C. Schatz, J. T. Hupp, O. K. Farha, T. J. Savenije, M. G. Kanatzidis and F. C. Grozema, Effect

- of Cation Rotation on Charge Dynamics in Hybrid Lead Halide Perovskites, *J. Phys. Chem. C*, 2016, **120**, 16577–16585.
- 73 Z. Guo, J. S. Manser, Y. Wan, P. V. Kamat and L. Huang, Spatial and Temporal Imaging of Long-Range Charge Transport in Perovskite Thin Films by Ultrafast Microscopy, *Nat. Commun.*, 2015, **6**, 7471.
- 74 H. Oga, A. Saeki, Y. Ogomi, S. Hayase and S. Seki, Improved Understanding of the Electronic and Energetic Landscapes of Perovskite Solar Cells: High Local Charge Carrier Mobility, Reduced Recombination, and Extremely Shallow Traps, *J. Am. Chem. Soc.*, 2014, **136**, 13818–13825.
- 75 J. Lim, M. T. Hörantner, N. Sakai, J. M. Ball, S. Mahesh, N. K. Noel, Y.-H. Lin, J. B. Patel, D. P. McMeekin, M. B. Johnston, B. Wenger and H. J. Snaith, Elucidating the Long-Range Charge Carrier Mobility in Metal Halide Perovskite Thin Films, *Energy Environ. Sci.*, 2019, **12**, 169–176.
- 76 C. Wehrenfennig, G. E. Eperon, M. B. Johnston, H. J. Snaith and L. M. Herz, High Charge Carrier Mobilities and Lifetimes in Organolead Trihalide Perovskites, *Adv. Mater.*, 2014, **26**, 1584–1589.
- 77 M. Karakus, S. A. Jensen, F. D'Angelo, D. Turchinovich, M. Bonn and E. Cánovas, Phonon–Electron Scattering Limits Free Charge Mobility in Methylammonium Lead Iodide Perovskites, *J. Phys. Chem. Lett.*, 2015, **6**, 4991–4996.
- 78 J. Zhou, N. Lei, H. Zhou, Y. Zhang, Z. Tang and L. Jiang, Understanding the Temperature-Dependent Charge Transport, Structural Variation and Photoluminescent Properties in Methylammonium Lead Halide Perovskite Single Crystals, *J. Mater. Chem. C*, 2018, **6**, 6556–6564.
- 79 S. Shrestha, G. J. Matt, A. Osvet, D. Niesner, R. Hock and C. J. Brabec, Assessing Temperature Dependence of Drift Mobility in Methylammonium Lead Iodide Perovskite Single Crystals, *J. Phys. Chem. C*, 2018, **122**, 5935–5939.
- 80 L. Z. Tan, F. Zheng and A. M. Rappe, Intermolecular Interactions in Hybrid Perovskites Understood from a Combined Density Functional Theory and Effective Hamiltonian Approach, *ACS Energy Lett.*, 2017, **2**, 937–942.
- 81 B. Li, Y. Kawakita, Y. Liu, M. Wang, M. Matsuura, K. Shibata, S. Ohira-Kawamura, T. Yamada, S. Lin, K. Nakajima and S. F. Liu, Polar Rotor Scattering as Atomic-Level Origin of Low Mobility and Thermal Conductivity of Perovskite  $\text{CH}_3\text{NH}_3\text{PbI}_3$ , *Nat. Commun.*, 2017, **8**, 16086.
- 82 L. P. Kadanoff, Boltzmann Equation for Polarons, *Phys. Rev.*, 1963, **130**, 1364–1369.
- 83 S. G. Christov, Adiabatic Polaron Theory of Electron Hopping in Crystals: A Reaction-Rate Approach, *Phys. Rev. B: Condens. Matter Mater. Phys.*, 1982, **26**, 6918–6935.